

A linear stability analysis of stratocumulus convection driven by radiative cooling

By PHILIP AUSTIN, *Programme in Atmospheric Science, #217 West Mall, University of British Columbia, Vancouver, British Columbia, V6T 1Z2, Canada*

(Manuscript received 14 May 1993; in final form 2 May 1994)

ABSTRACT

Fully cloudy stratocumulus layers sometimes exhibit convective organization at a single dominant length scale with an aspect ratio (width/height) ≈ 1 . We present a linear stability analysis of a radiatively-cooled cloud beneath a capping inversion and show that small aspect ratio modes are energetically favored over a broad range of inversion strengths and cooling depths. The integrated mode energy budgets indicate that, given a vertically limited region of radiative cooling, highly dissipative, localized convective modes can grow through efficient buoyancy production beneath the inversion. Including the effect of decoupling on the sub-cloud layer enhances this scale selection, but as the depth of the unstable layer is increased beyond 20% of the boundary layer depth, the critical Rayleigh number and the aspect ratio of the fastest growing mode approach that of a layer capped by a no-slip rigid lid.

1. Introduction

A series of observations has shown that convective plumes of descending cold air produced by radiative cooling at cloud top tend to be spaced at regular intervals in some stratocumulus clouds. Nicholls and Leighton (1986) observed hexagonally shaped patterns in the top of a solid sheet of stratocumulus cloud with a horizontal length scale of ≈ 1 km and an aspect ratio (width/height) of approximately one. Balloon observations by Caughey and Kitchen (1984) show regularly spaced downdrafts near cloud base with a horizontal spacing of 500–750 m and an aspect ratio of 0.5–0.75 (see Fig. 1). Nicholls (1989) reported the observation of conditionally sampled downdrafts in five flights through solid stratocumulus cloud, and showed that the downdraft spacing was consistent with horizontal penetrations through a randomly oriented field of hexagonal cells with a mean aspect ratio of 0.5 to 0.75. This length scale is also typical of the plume spacing found in large-eddy simulations of stratocumulus convection driven by a combination of cloud-top cooling and surface fluxes (Moeng and Schuman, 1991a).

While gravity waves trapped in the inversion layer may produce wave-like features at cloud top (Carruthers and Moeng, 1986), the three-dimensional character of the patterns seen by Nicholls suggests that convective scale selection can also play a role. Theoretical and laboratory studies of parallel plate convection have shown that the stability of a quiescent base state to infinitesimal perturbations can yield useful information about the preferred aspect ratio and vertical mode profile of finite amplitude perturbations. A radiatively cooled stratocumulus cloud is substantially more complicated than any laboratory analog, but the observed convective regularity indicates that a coherent circulation can at times dominate in these clouds. We will assume here that the laboratory model of growing perturbations on a marginally unstable base state has validity for at least some instances of radiatively driven convection at cloud top, and will focus on the influence exerted by a cloud top inversion on the most rapidly growing linear modes.

Below we develop linearized equations for the energy and velocity perturbations, given an inversion-capped base state that is unstable over a

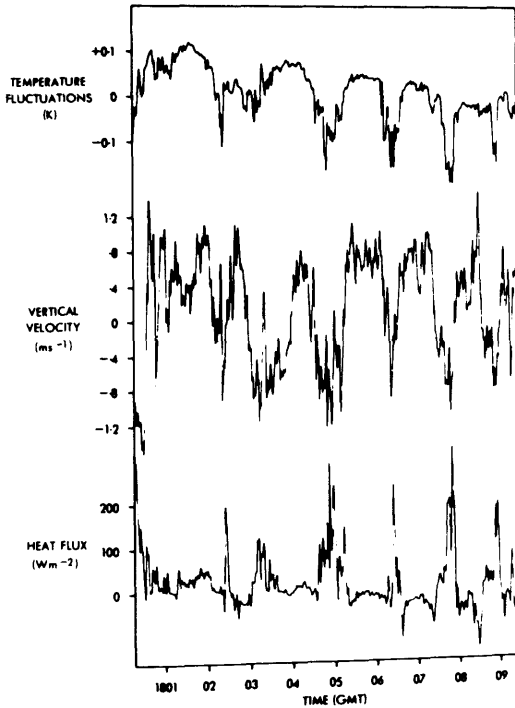


Fig. 1. (a) Tethered balloon measurements of T' , w' , and $T'w'$ near cloud base on 26 October 1977, at 1800 hours local time (GMT). One minute \approx 400 m (from Caughey and Kitchen, 1984, reprinted courtesy of the Royal Meteorological Society).

vertically limited region near cloud top. The perturbation equations include the thermodynamic effect of vertical transitions between cloud and clear air. Our objective is to show how an overlying stable layer can suppress radiatively-driven convection at scales larger than the layer depth, and promote convection at the length scales observed by Caughey and Kitchen (1984) and Nicholls (1989). The depth of the radiatively cooled layer, the inversion strength and the vertical profile of cloud water are interdependent, but we will use sensitivity tests to demonstrate that small aspect-ratio convective modes are favored over a broad range of realistic values of these parameters. We will also use the volume-integrated energy budgets for growing modes to understand why the preferred aspect ratio for convection beneath an inversion is roughly one third the size of that for convection beneath a stress-free rigid lid.

In Section 2 we present the linearized Boussinesq equations for a radiatively cooled cloud layer, and discuss the representation of small-scale turbulence and moist thermodynamics. Section 3 contains sensitivity studies of the linear stability of the base state: (1) as a rigid lid is replaced by a cloud-top inversion and the depth of the unstable layer is varied; (2) as the inversion strength and thickness are changed; (3) as the cloud thickness is varied. Section 4 contains a discussion of these results.

2. Equations

2.1. Momentum

The Boussinesq equations are valid for the shallow convection (≈ 1 km) considered here (Mahrt, 1986; Bretherton, 1987). We define the buoyancy, b , relative to an adiabatic reference state in hydrostatic equilibrium with density $\bar{\rho}(z)$:

$$b = -g \frac{\rho - \bar{\rho}(z)}{\rho_0}, \tag{1}$$

where ρ_0 is a constant reference density and g is the acceleration of gravity. Denoting perturbations by primes and dimensional variables by hats, and neglecting the effects of rotation, the continuity equations for mass and momentum become:

$$\text{momentum: } \frac{D\hat{\delta}'}{Dt} = -\frac{1}{\rho_0} \hat{\nabla} \hat{\pi}' + \hat{b}' \mathbf{k} + (\hat{\nabla} \cdot \mathbf{v}) \hat{\delta}' \tag{2}$$

$$\text{continuity: } \hat{\nabla} \cdot \hat{\delta}' = 0 \tag{3}$$

Here π is pressure, the bold characters are vectors, $\mathbf{v} = u\mathbf{i} + v\mathbf{j} + w\mathbf{k}$ is the velocity and D/Dt is the total derivative with respect to time.

2.2. Viscosity parameterization

We assume in (2) that the effects of turbulence on scales smaller than the perturbation scale are independent of the perturbations, and can be parameterized by an eddy viscosity ν (and, for energy and water, an eddy diffusivity κ). This assumption is made by most investigators, both because it preserves the correspondence with laboratory convection, and because there is little observational evidence to suggest an alternative assumption. Above the cloud, in the stably

stratified inversion, the eddy diffusivity is usually assumed to approach zero (e.g., Koračín and Rogers, 1990). We will model the vertical transition from cloud layer to the stably stratified inversion by writing $\nu = \nu_0 \nu_f(z)$, $\kappa = \kappa_0 \kappa_f(z)$, where ν_0, κ_0 are constant below the inversion, and ν_f, κ_f are functions which decrease rapidly across the inversion.

Non-dimensionalization will remove ν_0 and κ_0 (but not the Prandtl number $Pr = \nu_0/\kappa_0$) from the linear analysis, and their magnitudes need to be considered only when we consider growing modes (Subsection 3.3.2) or try to estimate the actual Rayleigh number regime of the boundary layer (Subsection 4). Following Roach et al. (1982) and Laufersweiler and Shirer (1989) we can infer a value for the eddy diffusivity ν_0 due to turbulence on scales smaller than those of the convective eddies we are interested in (with dominant length scales of 500–1000 m), using the similarity relation:

$$\nu_0 = \varepsilon^{(1/3)}(\lambda)^{(4/3)}/15, \tag{4}$$

where ε is the dissipation rate and λ is the length scale. We will need to parameterize the effect on the convective modes of dissipation at length scales below about 200 m; using observed values of $\varepsilon \approx 10^{-3} \text{ m}^2 \text{ s}^{-3}$ and $\lambda \approx 100\text{--}200 \text{ m}$ (Caughey et al., 1982) gives eddy diffusivities in the range $3\text{--}8 \text{ m}^2 \text{ s}^{-1}$. We will assume $Pr = 1$, $\nu_0 = 5 \text{ m}^2 \text{ s}^{-1}$ when needed in the discussion below.

2.3. Energy and water perturbations

We will focus on a cloud layer dominated by radiative flux divergence at cloud top, with small surface fluxes of sensible and latent heat. In such a layer the buoyancy perturbation, b' can be expressed in terms of perturbations of two variables conserved for moist adiabatic processes in the absence of precipitation: the moist static energy \hat{s}_m and the total water mixing ratio \hat{r}_T . These are defined as:

$$\hat{s}_m = c_p \hat{T} + L \hat{r}_v + g z^2, \tag{5}$$

$$\hat{r}_T = \hat{r}_v + \hat{r}_1$$

where c_p is the heat capacity of moist air, L the latent heat at temperature \hat{T} , $g z^2$ the gravitational potential energy and \hat{r}_v, \hat{r}_1 the vapor and liquid mixing ratios. For a cloud with net radiative

flux divergence $\hat{H}(\hat{z}) = -(1/\hat{\rho}) d\hat{E}_n/d\hat{z}$ the two variables obey the conservation equations:

$$\frac{D\hat{s}_m}{Dt} = (\hat{\nabla} \cdot \kappa \hat{\nabla}) \hat{s}_m + \hat{H}, \tag{6}$$

$$\frac{D\hat{r}_T}{Dt} = (\hat{\nabla} \cdot \kappa \hat{\nabla}) \hat{r}_T, \tag{7}$$

where κ is the eddy diffusivity of energy and water. Although a precipitation source/sink could be included in (7), we will limit our analysis to non-precipitating clouds in this study.

We assume a horizontally uniform, saturated cloud layer with $\hat{r}_v = \hat{r}_s$, so that the only transitions between clear and cloudy air occur at cloud top (\hat{z}_t) and cloud base (\hat{z}_b). With these assumptions the buoyancy perturbations \hat{b}' of (2) can be related to perturbations in \hat{s}_m and \hat{r}_T through the virtual temperature \hat{T}_v or virtual dry static energy, \hat{s}_v (e.g., Randall, 1980):

$$\hat{b}' \approx g \frac{\hat{T}'_v}{T_{v0}} = g \frac{\hat{s}'_v}{s_{v0}} \approx \frac{g}{s_{v0}} (\beta_1 \hat{s}'_m + \beta_2 L \hat{r}'_T), \tag{8}$$

where $\hat{T}_v = \hat{T}(1 + 0.61\hat{r}_v - \hat{r}_1)$, $\hat{s}_v = c_p \hat{T}_v$ and the subscript $_0$ denotes a reference base state.

The coefficients β_1, β_2 are weak functions of temperature and pressure and non-linear functions of parcel saturation. Defining the derivative $\gamma = dr_s/dT$ gives:

$$\left\{ \begin{array}{l} \beta_1 = \frac{(1 + 1.61T_0\gamma)}{1 + (L/c_p)\gamma} \approx 0.6 \\ \beta_2 = -\frac{c_p T_0}{L} \approx -0.1 \end{array} \right\} \tag{9}$$

saturated perturbations,

$$\left\{ \begin{array}{l} \beta_1 = 1 \\ \beta_2 = \left(0.61 \frac{c_p T_0}{L} - 1 \right) \approx -0.9 \end{array} \right\} \tag{10}$$

unsaturated perturbations.

Where the approximate numerical values of the coefficients are chosen for a base-state T_0 of 280 K and π_0 of 950 hPa.

We seek to capture some of the important thermodynamic features represented by (8), (9) and (10) in a linear stability analysis. A linear represen-

tation of (9) and (10) can be obtained by assuming that buoyancy, moist static energy, and water perturbations are proportional to one another, with a proportionality constant α that varies with height in the layer, i.e.,

$$s'_v = \alpha(z) s'_m. \quad (11)$$

To determine the vertical dependence of α , we consider the relationship between perturbations of virtual static energy, moist static energy, and total water in a representative stratocumulus cloud driven by cloud top cooling. Models and observations (e.g., Moeng, 1986; Nicholls and Leighton, 1986; Moyer and Young, 1991; Moeng and Schumann, 1991a) indicate that towards the top of a radiatively-driven entraining cloud layer, the energy and water fluxes $w's'_m$, $Lw'r'_T$ produced by cool, comparatively dry downdrafts and compensating warm, moist updrafts are positive and roughly equal, with the water flux $Lw'r'_T$ decreasing linearly below cloud top through the cloud and sub-cloud layers, and the buoyancy flux $w's'_v$ often falling to zero at cloud base. Although the water flux is potentially large within cloud, the values of $\beta_1 \approx 0.6$, $\beta_2 \approx -0.1$ given in (9) indicate that total water perturbations produce a relatively small contribution to the buoyancy flux, for typical water and energy fluxes. In the subsaturated air below cloud the coefficients change to $\beta_1 \approx 1$, $\beta_2 \approx -0.9$ as the effect of phase change is removed. Here radiative heating and the shift from saturated to subsaturated thermodynamics can act to push $w's'_v$ to zero at cloudbase and decouple the cloud from the surface moisture flux (Turton and Nicholls, 1987). In contrast, above cloud in the dry inversion the strong, positive temperature gradient dominates, producing a negative buoyancy flux which damps velocity perturbations in the stable layer.

While this three-layer parameterization can capture only part of the non-linear thermodynamics that accompany entrainment and phase change, it does offer a way to represent the sharp vertical transition in the partitioning of energy perturbations into buoyancy and phase change at cloud top and base.

Summarizing values of α appropriate to the cloud, sub-cloud, and inversion layers:

Within cloud: The β values used in (9) suggest $\alpha_{\text{cloud}} \approx 0.5$, which will hold approximately as long

as the layer perturbations satisfy $Lr'_T \leq s'_m$. With this value of α_{cloud} , energy perturbations are partitioned evenly between temperature change and phase change.

Below cloud: $\alpha_{\text{sub-cloud}} \approx 0$. For the special case of a decoupled cloud layer, which is frequently observed in the late-afternoon marine boundary layer, we force the buoyancy flux to zero below cloud base. We test the sensitivity of the layer stability to cloud thickness under this assumption in Subsection 3.4.

Above cloud: $\alpha_{\text{inversion}} \approx 1$. In the subsaturated inversion the virtual static energy is approximately conserved, and both the virtual and moist energy perturbations are dominated by strong inversion gradients, i.e.,

$$s'_v \approx w' \frac{ds'_v}{dz}, \quad s'_m \approx w' \frac{ds'_m}{dz}. \quad (12)$$

Eq. (12) suggests a value of

$$\alpha_{\text{inversion}} = \frac{ds'_v/dz}{ds'_m/dz},$$

which will be in the range $\alpha_{\text{inversion}} = 1-1.5$ provided the total water deficit is modest (1-3 g/kg) in the dry layer. Larger negative gradients in total water are often observed above stratocumulus; these can force $ds'_m/dz \leq 0$ despite a strongly stable temperature gradient. The inversion is still absolutely stable in this case, but in the subsaturated layer β_1 and β_2 are of similar magnitude, and the gradient $d\bar{r}'_T/dz$ would have to be included in (12) when $|ds'_m/dz| \approx |d\bar{r}'_T/dz|$.

The use of (11) with these choices for α eliminates the conservation equation for total water. In contrast to a "dry cloud" approximation (e.g., Lilly, 1968), however, the impact of phase change is retained. Within the cloud, where $\alpha(z) = \alpha_{\text{cloud}} \approx 0.5$, half of the energy perturbation is used to evaporate or condense water, and is unavailable to change the temperature (or buoyancy). As a result, more energy is required to produce the buoyancy deficit needed to initiate and drive convection than in a fluid that doesn't undergo phase change.

Figs. 2a, 2b show profiles of \bar{T} , \bar{r}_1 , \bar{r}_T and \bar{s}_m , for the upper portion of a representative cloud layer. A 230 m thick cloud, with a linear liquid water profile that is 80% of adiabatic, is capped by a

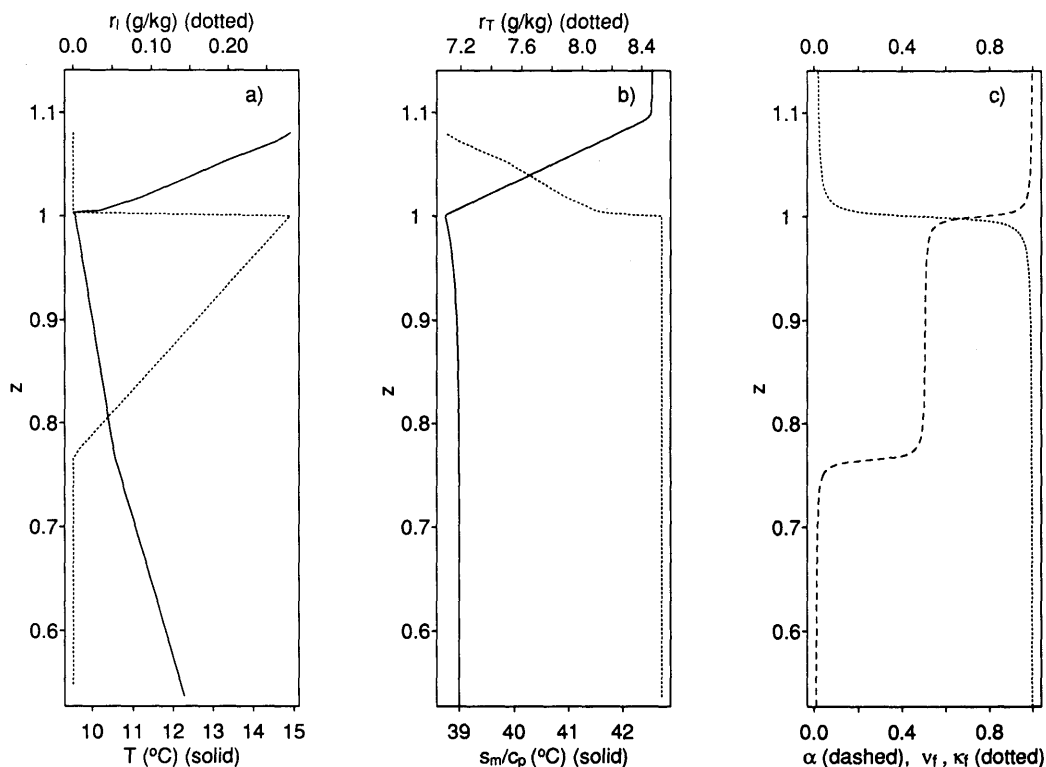


Fig. 2. Idealized thermodynamic profiles for a stratocumulus cloud. (a) Temperature T ($^{\circ}\text{C}$, solid), liquid water mixing ratio r_l (g/kg dotted). (b) moist static energy s_m/c_p ($^{\circ}\text{C}$, solid), total water mixing ratio r_T (g/kg , dotted). Above cloud inversion strength is $f_b = 2 \times 10^{-3} \text{ s}^{-2}$ c) shape functions for the thermodynamic coefficient α_f (dashed), and the eddy diffusivity and conductivity v_f, κ_f (dotted) with a cloud-top transition of $dv_f/dz = d\alpha_f/dz = -100$.

temperature inversion of $6 \text{ K}/100 \text{ m}$, corresponding to a Brunt-Väisälä frequency

$$f_b \equiv \frac{g}{\theta_v} \frac{d\theta_v}{dz} \approx 2 \times 10^{-3} \text{ s}^{-2}.$$

In the remainder of the upper layer, this inversion is relaxed to $(1/c_p) d\bar{s}_m/dz = 0.05 \text{ K}/100 \text{ m}$; the results presented below are not sensitive to the strength of the inversion in the upper part of the domain. The inversion is moderately dry, with a total moisture decrease of $1.5 \text{ g}/\text{kg}$ across the 100 m above cloud.

Fig. 2c shows the shape functions $\alpha(z)$ and $v_f = \kappa_f$ that represent the cloud-base and cloud top transitions in the eddy viscosity/diffusivity and the moist/dry thermodynamics. These transitions are fit with matched arctangents; the derivatives $d\alpha/dz = dv_f/dz$ have a non-dimensional value of

-100 at $z = 1.0$ in Fig. 2c. This means that, for example, in a 1000 m deep layer the viscosity shape function v_f varies from 1 to 0 in approximately 10 m . Balloon measurements of the temperature and turbulence profiles across cloud top indicate that this is a representative length for the transition between cloud and inversion (Caughey et al., 1982). Horizontal undulations in the cloud/inversion interface on scales smaller than the convective wavelength could produce a deeper effective transition; we will explore the sensitivity of the mode stability to $f_b, v_f,$ and α in Subsection 3.3 below.

We decompose the thermodynamic variables into horizontally averaged and perturbation components: $\hat{s}_m = \bar{s}_m(z) + s'_m$. We will assume that the horizontally averaged base state changes slowly compared with the growth of the initially unstable modes, and is shaped by the mean radiative heat-

ing profile and the diffusive action of turbulent eddies smaller than the perturbations:

$$(\hat{\nabla} \cdot \kappa \hat{\nabla}) \overline{\delta'_m} = -\overline{\hat{H}}. \tag{13}$$

The vertical extent of the unstable layer will be approximately set by the cooling depth through (13); we will use an exponential fit to $\overline{\hat{H}}$ and estimate the size of the decay scale in Section 2.4 below. Above cloud we will specify $\overline{\delta'_m}$, and test the effects of inversion strength on layer stability.

Subtracting (13) from (6) yields the perturbation equation for the energy:

$$\frac{D\delta'_m}{Dt} = (\hat{\nabla} \cdot \kappa \hat{\nabla}) \delta'_m + \hat{H}'. \tag{14}$$

The quantity \hat{H}' consists of perturbations in absorption or emission within the cloud due to perturbations in liquid water and cloud temperature. Bakan (1982) included the effect of radiative heat exchange and optical depth perturbations in a linear stability analysis of convection beneath a rigid lid. He found the radiative interactions to be small and slightly destabilizing, acting to increase the critical aspect ratio (width/height of the fastest growing mode) by $\approx 4\%$. Fiedler (1984) included a linear dependence of the flux divergence on cloud

thickness in a stability analysis that coupled cloud thickness perturbations to both radiative cooling and the entrainment energetics of the cloud and inversion, and also found little effect for optically thick cloud. We will consider only optically thick (depth greater than 200 m) clouds in the analysis below and neglect \hat{H}' in (14).

2.4. The base state energy profile

We now scale the depth of the cloud-top cooling layer based on Hansen and Derr's (1987) parameterization of the net-flux profile E_n . They showed that, within a cloud in which the liquid water increases linearly with height, E_n can be fit by the sum of three exponential functions with different vertical decay scales:

$$\begin{aligned} \hat{E}_N = & \hat{E}_{0s} + \hat{E}_{Nl} \exp\left(\frac{-(\hat{z} - \hat{z}_b)}{\hat{\lambda}_1}\right) \\ & + \hat{E}_{Nu} \exp\left(\frac{-(\hat{z}_t - \hat{z})}{\hat{\lambda}_u}\right) \\ & + \hat{E}_{Ns} \left(1 - \exp\left(\frac{-(\hat{z}_t - \hat{z})}{\hat{\lambda}_s}\right)\right). \end{aligned} \tag{15}$$

The subscripts l, u, and s denote the contributions due to long wave radiation in the upper and lower parts of the cloud and to shortwave radiation at cloud top, respectively, and \hat{z}_t and \hat{z}_b are the heights of cloud top and cloud base. The decay scales are functions of the total liquid water path W ; for the range $40 \text{ g m}^{-2} < W < 100 \text{ g m}^{-2}$ they span (m) $\hat{\lambda}_1 \approx 80$, $30 < \hat{\lambda}_s < 40$ and $7 < \hat{\lambda}_u < 22$. Fig. 3 shows the profiles of long and shortwave net flux given by (15) for cloud top fluxes matching a 01:30 GMT (18:30 local daylight time) aircraft sounding (NCAR Electra measurements from the First ISCCP Regional Experiment (see Albrecht et al., 1988)). The decay scales for this case (with $W = 44 \text{ g m}^{-2}$) are: $\hat{\lambda}_s = 33 \text{ m}$, $\hat{\lambda}_u = 17 \text{ m}$, $\hat{\lambda}_1 = 77 \text{ m}$. The profiles are characteristic of marine stratocumulus clouds with cloud bases between 500–700 m: the solar and cloud top long-wave fluxes are localized in the upper 75 m of the cloud and move through the course of a day from counteracting heating and cooling at cloud top to strong cloud top cooling. The cloud base heating, which depends on cloud base and sea surface temperatures, varies more slowly over the same period. Aircraft observations of the total net

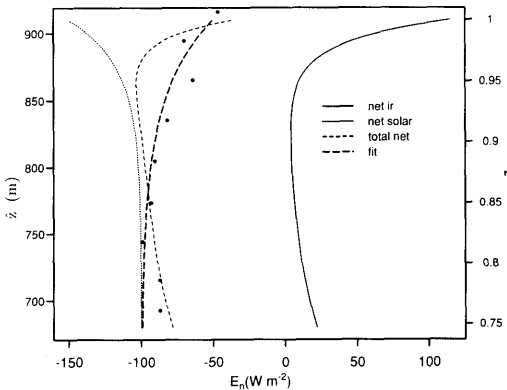


Fig. 3. Model fluxes ($W \text{ m}^{-2}$) using the exponential approximation of Hanson and Derr (1987) for net long-wave ($\hat{\lambda}_u = 17 \text{ m}$ (solid)), net solar ($\hat{\lambda}_s = 33 \text{ m}$ (dotted)), and total net upward flux (dot-dashed), for cloud top fluxes measured at 1:30 GMT (18:30 PDT) on 2 July, 1987. The dots show vertically averaged total net flux measurements in cloud from NCAR Electra aircraft data, while the heavy dashed curve is an exponential cooling profile with $\hat{\lambda} = 50 \text{ m}$.

flux, averaged vertically over 30 m intervals, are included as dots in Fig. 3. Although the accuracy of radiometric data from this rolling platform is questionable, the points suggest that a larger decay scale may be applicable to this cloud (an exponential \hat{E}_n curve with $\hat{\lambda} = 50$ m is shown for comparison). We will focus here on radiatively induced changes to \bar{s}_m near cloud top produced by a range of radiative cooling profiles, and assume that the long and short wave flux divergence and the eddy diffusion generates an unstable base state $\bar{s}_m(z)$ with a single decay scale $\hat{\lambda}$ and an exponential dependence below the inversion of the form of (15):

$$\bar{s}_m = \frac{-\Delta s_m \exp(-(\hat{z}_t - \hat{z})/\hat{\lambda})}{(1 - \exp(-\hat{z}_t/\hat{\lambda}))} \tag{16}$$

Note from (16) that the total energy change across

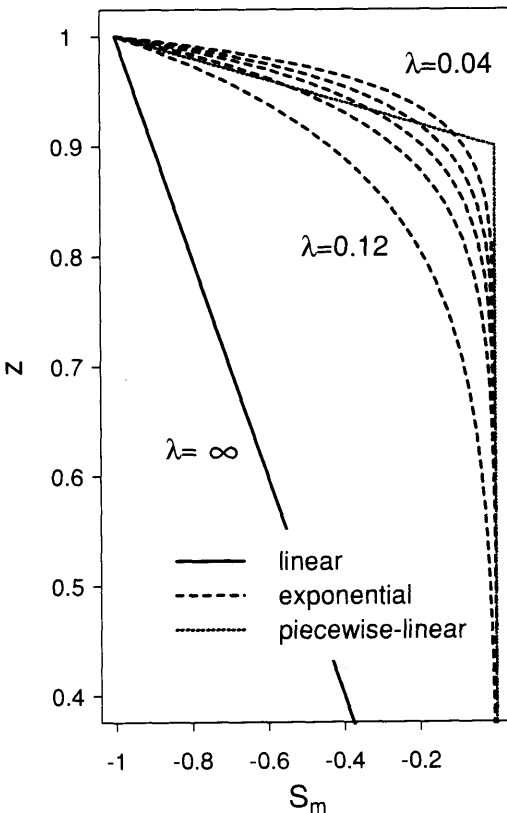


Fig. 4. Three forms of the base-state \bar{s}_m . Linear ($\lambda = \infty$) (solid), exponential (see (16)) with $\lambda = 0.04, 0.05, 0.06, 0.075, 0.12$ (dashed); piecewise-linear (dotted).

the boundary layer is given by $\bar{s}_m(\hat{z}_t) - \bar{s}_m(0) = -\Delta s_m$.

We will investigate the effect on perturbation stability of a base state temperature profile characterized by a single length scale $\hat{\lambda}$ in the range $40 \text{ m} < \hat{\lambda} < 120 \text{ m}$ in Section 3 below. Fig. 4 shows this curve family, with $\hat{\lambda}$ non-dimensionalized by the inversion height z_i , as well as a linear ($\lambda = \infty$) and a piecewise-linear base state. The piecewise-linear profile permits an analytic solution. It also provides a check on the sensitivity of the stability analysis to the details of the profile shape; the unstable modes found in Section 3 exhibit the same critical aspect ratios for both exponential and piecewise-linear base states of similar length scales.

2.5. Linearized equations with latent heating

We non-dimensionalize (2) and (14) with the inversion height \hat{z}_t and the diffusive time \hat{z}_t^2/κ . From (16) and (8), the total buoyancy difference between cloud and surface for a base state in which the instability is confined to the cloud is given by $g \Delta T_v/T_{v0} = g \alpha_{\text{cloud}} \Delta s_m/s_{v0}$. This buoyancy difference is used to non-dimensionalize the buoyancy perturbation in (2); we will write $\alpha(z)$ as $\alpha_{\text{cloud}} \alpha_f(z)$ below. The pressure perturbation is removed by cross-differentiating the components of (2) and (3) and subtracting, and the buoyancy is related to the moist static energy through (8) and (11), which yields:

$$\left(\frac{\partial}{\partial t} - v_f \text{Pr} \nabla^2 - \text{Pr} \frac{dv_f}{dz} \frac{\partial}{\partial z} \right) \nabla^2 w' - \text{Pr} \frac{d^2 v_f}{dz^2} \frac{\partial^2 w'}{\partial z^2} = \text{Ra Pr} \nabla_H^2 \alpha_f s'_m, \tag{17}$$

$$\left(\frac{\partial}{\partial t} - (\nabla \cdot \kappa_f \nabla) \right) s'_m = -\frac{d\bar{s}_m}{dz} w', \tag{18}$$

with the Rayleigh and Prandtl numbers given by:

$$\text{Ra} = \frac{-gz_t^3 \alpha_{\text{cloud}} \Delta s_m}{s_{v0} v_0 \kappa_0}, \tag{19}$$

$$\text{Pr} = \frac{v_0}{\kappa_0}.$$

Below we set $\text{Pr} = 1$, and $\kappa_f = v_f$, i.e., the diffusivity of both momentum and buoyancy will be similarly restricted by the stable inversion.

Eqs. (17) and (18) are separable with solutions of the form:

$$\begin{bmatrix} w' \\ s'_m \end{bmatrix} = \begin{bmatrix} w(z) \\ s_m(z) \end{bmatrix} \exp[\sigma t + i\mathbf{k} \cdot \mathbf{x}], \tag{20}$$

where σ is the growth rate and $\mathbf{k} = (k_x \hat{i} + k_y \hat{j})$, $k^2 = k_x^2 + k_y^2$ is the horizontal wavenumber of the perturbation (planform unspecified). Inserting this into (17) and (18) gives:

$$\begin{aligned} & \left(\sigma - v_f \text{Pr} \left(\frac{d^2}{dz^2} - k^2 \right) - \text{Pr} \frac{dv_f}{dz} \frac{d}{dz} \right) \left(\frac{d^2}{dz^2} - k^2 \right) w \\ & - \text{Pr} \frac{d^2 v_f}{dz^2} \frac{d^2 w}{dz^2} = -\text{Ra} \text{Pr} k^2 \alpha_f s_m \end{aligned} \tag{21}$$

and:

$$\begin{aligned} & \left(\alpha - v_f \left(\frac{d^2}{dz^2} - k^2 \right) - \frac{dv_f}{dz} \frac{d}{dz} \right) s_m \\ & = -\frac{ds_m}{dz} w. \end{aligned} \tag{22}$$

Using (8), (11), (21) and (22), we can write a single sixth-order ordinary differential equation in z :

$$\begin{aligned} & \left(\sigma - v_f \left(\frac{d}{dz^2} - k^2 \right) - \frac{dv_f}{dz} \frac{\partial}{\partial z} \right) \\ & \times \left[\left(\alpha - \text{Pr} v_f \left(\frac{d}{dz^2} - k^2 \right) \right) \left(\frac{d}{dz^2} - k^2 \right) w \right. \\ & - \text{Pr} \frac{dv_f}{dz} \left(\frac{d^2}{dz^2} - k^2 \right) \frac{dw}{dz} \left. \right] \\ & = \text{Ra} \text{Pr} k^2 \left(\alpha_f \frac{ds_m}{dz} w + 2v_f \frac{d\alpha_f}{dz} \frac{ds_m}{dz} \right. \\ & \left. + v_f \frac{d^2 \alpha_f}{dz^2} s_m + \frac{\partial v_f}{\partial z} \frac{\partial \alpha_f}{\partial z} s_m \right), \end{aligned} \tag{23}$$

where the perturbation $s_m(z)$ is determined from $w(z)$ and its derivatives through (21), and the derivative ds_m/dz is found by differentiating (21) with respect to z . Eq. (23) reduces to the usual linear stability equation when $v_f(z) = \kappa_f(z) = \alpha_f(z) = 1$; the last three terms on the rhs arise from diffusion operating on the buoyancy perturbation $b(z) = \alpha(z) s_m(z)$.

We will use a rigid, free-slip lower boundary ($w = d^2w/dz^2 = 0$ at z_{bot}), and either a rigid free-

slip or no-slip ($w = dw/dz = 0$ at z_{top}) upper boundary. We also require that the boundaries be conducting ($s_m(z_{\text{top}}) = s_m(z_{\text{bot}}) = 0$); from (21) this is equivalent to:

$$w(z_{\text{bot}}) = \frac{d^2 w}{dz^2} \Big|_{z_{\text{bot}}} = \frac{d^4 w}{dz^4} \Big|_{z_{\text{bot}}} = 0, \tag{24}$$

if the boundary is rigid and free-slip. (Note from Fig. 2c that $dv_f/dz = 0$ at the boundaries.)

Setting $\sigma = 0$ and solving (23) for the eigenfunction $w(z)$ (and eigenvalue Ra) as a function of the wavenumber k gives the neutral stability curve. Curve values identify the critical Rayleigh number (Ra_{crit}) required to initiate convection, and the non-dimensional wavelength of the smallest Ra_{crit} gives the aspect ratio of the most unstable mode ($a_{\text{crit}} = 2\pi/k_{\text{crit}}$). We use a shooting technique to find these eigenvalues, starting at the upper boundary with values for the perturbation velocity and its first five derivatives:

$$\begin{aligned} \mathbf{w}_i(z_{\text{top}}) &= [w_i(z_{\text{top}}) \quad w_i^{(1)}(z_{\text{top}}) \quad w_i^{(2)}(z_{\text{top}}) \\ & w_i^{(3)}(z_{\text{top}}) \quad w_i^{(4)}(z_{\text{top}}) \quad w_i^{(5)}(z_{\text{top}})], \end{aligned} \tag{25}$$

where the superscripts denote the order of the derivative and the subscript $i = (1, 2, 3)$ indicates that we use three independent initial conditions to produce three orthogonal \mathbf{w}_i vectors. The boundary conditions are met at z_{top} for each \mathbf{w}_i , and the three solutions are then integrated downward using a 4th order Runge-Kutta scheme, with Gram-Schmidt orthogonalization employed at every step to keep the solutions linearly independent (Conte, 1969). We require that a linear combination of these three solutions satisfy the rigid, free-slip, conducting boundary conditions at z_{bot} . Writing the coefficients for the linear combination as γ_i and explicitly noting the dependence of the solutions on the Ra eigenvalue gives for (24):

$$\begin{aligned} & \gamma_1 w_1(z_{\text{bot}}, \text{Ra}) + \gamma_2 w_2(z_{\text{bot}}, \text{Ra}) \\ & + \gamma_3 w_3(z_{\text{bot}}, \text{Ra}) = 0, \\ & \gamma_1 w_1^{(2)}(z_{\text{bot}}, \text{Ra}) + \gamma_2 w_2^{(2)}(z_{\text{bot}}, \text{Ra}) \\ & + \gamma_3 w_3^{(2)}(z_{\text{bot}}, \text{Ra}) = 0, \\ & \gamma_1 w_1^{(4)}(z_{\text{bot}}, \text{Ra}) + \gamma_2 w_2^{(4)}(z_{\text{bot}}, \text{Ra}) \\ & + \gamma_3 w_3^{(4)}(z_{\text{bot}}, \text{Ra}) = 0, \end{aligned} \tag{26}$$

at a particular wavenumber k .

A solution to (26) exists only if the determinate of the coefficients of (26) vanishes; to find the eigenvalue that satisfies this condition (23) is solved for varying Ra until the three orthogonal solutions give:

$$\begin{vmatrix} w_1(z_{\text{bot}}, \text{Ra}) & w_2(z_{\text{bot}}, \text{Ra}) & w_3(z_{\text{bot}}, \text{Ra}) \\ w_1^{(2)}(z_{\text{bot}}, \text{Ra}) & w_2^{(2)}(z_{\text{bot}}, \text{Ra}) & w_3^{(2)}(z_{\text{bot}}, \text{Ra}) \\ w_1^{(4)}(z_{\text{bot}}, \text{Ra}) & w_2^{(4)}(z_{\text{bot}}, \text{Ra}) & w_3^{(4)}(z_{\text{bot}}, \text{Ra}) \end{vmatrix} = 0. \tag{27}$$

The eigenvalue found by solving (27) will be the critical Rayleigh number Ra_{crit} . We solve (27) for a range of aspect ratios to find the minimum Ra_{crit} and the corresponding a_{crit} of the most unstable mode. With a linear $\alpha \bar{s}_m$ profile (see solid line, Fig. 4) and free-slip boundaries the minimum Ra is $\text{Ra}_{\text{crit0}} = 27\pi^4/4 \approx 657$; it occurs at $a_{\text{crit}} \approx 2.8$. With one free-slip and one no-slip boundary and the same linear base state, convection begins at the minimum Rayleigh number $\text{Ra}_{\text{min}} = 1.7 \text{Ra}_{\text{crit0}}$, at an aspect ratio $a_{\text{crit}} \approx 2.1$. Once the eigenvalue is found, the appropriate γ_s can be determined from (26) and vertical profiles can be constructed of $w(z)$, its derivatives, and, (through (21)) $s_m(z)$.

We can also examine the behavior of growing modes by fixing Ra at a value larger than the neutral Ra_{crit} value found above. In this case the growth rate σ becomes the eigenvalue. We will show the relation of σ to the vertically integrated profiles of $w(z)$ and $s_m(z)$ in Subsection 2.7.

2.6. Thermal boundary conditions

The impact of partially or completely insulating, rigid boundaries on the preferred aspect ratio of parallel-plate convection has been studied by several investigators (e.g., Hurle et al., 1967). They found that reducing the thermal diffusivity κ_s for the solid boundary increases the preferred aspect ratio of the fastest-growing mode, because the bulk of the buoyancy change now takes place in a relatively deep layer within the boundary. The long horizontal traverse of the convective circulation at the layer top can be made without any buoyancy loss for a nonconducting boundary, and large-scale, less dissipative modes will have a significant advantage. Sasaki (1970) used boundary conditions which included insulation in the form of a variable Newtonian cooling term at the upper and lower boundaries. He found signifi-

cantly larger critical aspect ratios for an insulating layer, and suggested this as an explanation for the large aspect ratios ($a = 15\text{--}30$) observed in mesoscale cellular convection.

Below we will identify features of a cloud-capped inversion that *reduce* the size of convective modes to the observed aspect ratio of $\approx 0.5\text{--}0.75$. For this reason, comparisons between a realistic inversion and a perfectly conducting rigid lid are conservative, since, as the studies with partially conducting boundaries indicate, a conducting boundary produces the smallest possible convective mode for a base state capped by a rigid lid. We will use the conducting rigid lid as a benchmark against which to test the impact of a cloud-top inversion on mode aspect ratio in Section 3.

2.7. Mode energy budgets

To highlight the processes governing the scale selection of the fastest growing mode, it is useful to look the energy budget of modes forced by $\text{Ra} > \text{Ra}_{\text{crit}}$ with eigenvalues $\sigma > 0$. Taking the dot product of the linearized version of (2) and the velocity, and integrating over the vertical domain and the horizontal wavelength yields the volume integrated kinetic energy:

$$\begin{aligned} \frac{\partial E_k}{\partial t} &= \sigma E_k = \int_V \mathbf{v}' \cdot \frac{\partial \mathbf{v}'}{\partial t} dV = \text{Ra Pr} \int_V w' b' dV \\ &+ \text{Pr} \int_V \mathbf{v}' \cdot (\nabla \cdot \mathbf{v}_f \nabla) \mathbf{v}' dV, \end{aligned} \tag{28}$$

or, normalizing by E_k :

$$\begin{aligned} \sigma &= \frac{\text{Ra Pr}}{E_k} \int_V w' b' dV \\ &+ \frac{\text{Pr}}{E_k} \int_V \mathbf{v}' \cdot (\nabla \cdot \mathbf{v}_f \nabla) \mathbf{v}' dV, \end{aligned} \tag{29}$$

$$\sigma = \int p(z) dz + \int d(z) dz = P + D.$$

We will refer to $p(z)$ and $d(z)$ as the buoyancy production and the dissipation efficiencies, and P and D (< 0) as the integrated production and dissipation. Note that the pressure perturbation term in (2) vanishes due to the rigid boundaries at domain top and bottom.

At fixed Ra and wavenumber k (or aspect

ratio a), (23) can be solved for the eigenvalue σ , and P and D can be computed for the mode eigenfunctions $w(z)$ and $s_m(z)$. We will use (29) to compare the mechanisms causing mode growth or damping as we change boundary conditions at a particular (a, Ra) . The maximum growth rate σ for a particular forcing Ra will occur at an aspect ratio which is a compromise between large dissipation due to diffusion across the small horizontal and vertical wavelengths, and low buoyancy production at large wavelengths, where significant time is spent in horizontal transport without energy transfer to the perturbations through the $w' d\bar{s}_m/dz$ term in (18).

3. Results

The linearized perturbation equation (23) requires specification of the base state cooling depth through λ , the inversion strength through the value of $d\bar{s}_m/dz$, and the inversion thickness through the profiles v_f and α_f . Clearly these parameters are tightly coupled; for example Siems et al. (1993) have used a one dimensional mixed layer model below a subsiding upper layer to show the impact of inversion vapor content and subsidence rate on the cloud top radiative flux. Our approach is to examine the neutral stability of the layer for a range of realistic choices of \bar{s}_m , α_f , and v_f . While we can't predict particular combinations of these parameters without a full model of the base-state evolution, we can show that a preference for small-aspect ratio modes is characteristic of a broad range of (λ, \bar{s}_m) values, and we can contrast these modes to those generated beneath a rigid upper boundary.

3.1. Cooling beneath a rigid lid

Fig. 5 shows the neutral stability curves found by solving for the eigenvalue Ra in (23) with the growth rate σ set to zero. The curves identify the forcing required to initiate convection for a particular aspect ratio and set of boundary conditions. Positive growth rates $\sigma > 0$ will be produced for Ra larger than the Ra_{crit} given by the neutral curves. There are three sets of curves in the figure: solid lines give the stability of a linear ($\lambda = \infty$) base state for a free-slip (1) and no-slip (2) upper boundary; dotted lines compare the stability of a piecewise-linear unstable layer (3) (see the dotted line,

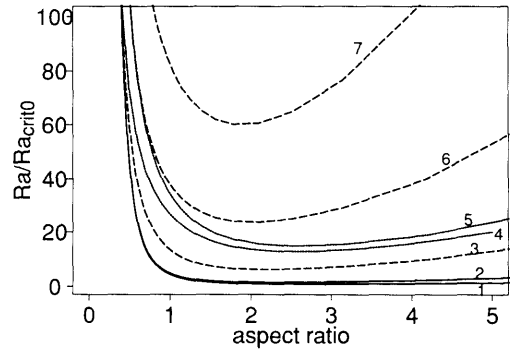


Fig. 5. Marginal stability curves for a rigid, conducting free-slip or no-slip boundary at $z = 1$ and a rigid, conducting, free-slip boundary at $z = 0$, with various values of the length-scale λ for the base-state \bar{s}_m shown in Fig. 4: (1) linear ($\lambda = \infty$), free-slip, $a_{crit} = 2.8$; (2) linear, no-slip, $a_{crit} = 2.5$; (3) exponential, $\lambda = 0.12$, no-slip, $a_{crit} = 2.1$; (4) piece-wise linear, free-slip, $a_{crit} = 2.6$; (5) exponential, $\lambda = 0.04$, free-slip, $a_{crit} = 2.5$; (6) exponential, $\lambda = 0.06$, no-slip, $a_{crit} = 2.1$; (7) exponential, $\lambda = 0.04$, no-slip, $a_{crit} = 1.9$. All curves scaled by $Ra_{crit0} = 657$.

Fig. 4) and an exponential base state (4, $\lambda = 0.04$) for a free-slip upper boundary; and the dashed lines show the stability of exponential base states for three different unstable length scales ((5) $\lambda = 0.12$, (6) $\lambda = 0.06$, (7) $\lambda = 0.04$) with a no-slip rigid lid.

The figure caption lists the accompanying critical aspect ratio, a_{crit} for which Ra_{crit} is minimum, for each base state. While the critical Rayleigh number increases as the vertical depth of the instability decreases, there is relatively little impact of cooling depth on the base state critical aspect ratio. Each of the base states has a preferred aspect ratio greater than 1.9, with shifts in cooling depth from $\lambda = \infty$ to $\lambda = 0.04$ producing less than a 10% change in a_{crit} (see lines 3, 6, 7). Fig. 5 also provides an illustration of the general result that the mode convection is not sensitive to the details of vertical profile of \bar{s}_m ; exponential and piece-wise linear base states (4) and (5) produce nearly identical critical aspect ratios for the same approximate cooling depth, and replacing the exponential base states 3, 6, 7 with piece-wise linear unstable layers of depths 70, 90, and 150 m respectively also yield similar stability curves (not shown).

We can use the mode energy budgets at large and small aspect ratios to identify the mechanisms

responsible for damping the growth at large horizontal scales under a no-slip inversion. In Fig. 6 we display the mode buoyancy and velocity perturbations for two growing modes with Ra fixed at $100 Ra_{crit}$, cooling depth $\lambda=0.06$ and aspect ratios of 2 and 0.8, respectively. The figure shows the buoyancy $b(z)$ and the vertical velocity $w(z)$, normalized so that the integrated fluxes calculated from these curves produce the buoyancy production P and the dissipation D defined in (29). P , D and the resulting growth rate $\sigma = P + D$ are listed on the figures, and the \bar{s}_m profile (with $\lambda = 0.06$) is shown as a dashed line to give the vertical scale of the cooling depth.

Comparing the no-slip (upper) and free-slip

(lower) boundaries in Fig. 6a shows that the no-slip boundary forces the velocity perturbation away from the rigid lid and out of the radiative cooled layer when $a=2$. For the smaller aspect ratio of panel 6b the effect is reversed; the maximum for the velocity perturbation has increased from $z=0.6$ in panel 6a to $z=0.76$. As a result, the buoyancy flux and the integrated buoyancy production P are more than a factor of two greater for $a=0.8$ than for the large aspect ratio mode. The smaller mode is more dissipative, but the increased buoyancy production results in a growth rate increase from $\sigma = 32$ to $\sigma = 45$.

3.2. Cooling beneath a cloud-top inversion

The effect of replacing the rigid lid with the inversion of Fig. 2 is shown in Fig. 7. In this section we will focus on the cloud-top inversion, extend cloud base to the surface, and take $\alpha(z) = \alpha_{cloud}$ from the inversion to the ground. The impact of an additional transition α at cloud base will be discussed in Subsection 3.4. The dashed lines reproduce two of the no-slip rigid lid stability curves from Fig. 5 for comparison; in the presence of an inversion all cooling depths have critical aspect ratios a_{crit} between 0.7 and 1.25. Large aspect ratio convection is suppressed, particularly for cooling layers that are limited to the upper portion of the boundary layer. For instance, in an inversion-capped cooling layer with $\lambda = 0.04$, at a convective forcing of $Ra = 200 Ra_{crit0}$, only modes with an

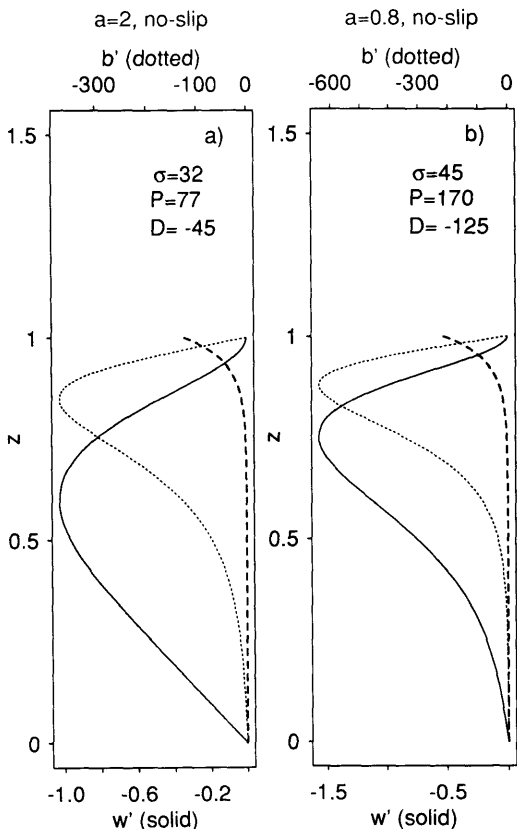


Fig. 6. Velocity and buoyancy perturbations $w(z)$, $b(z)$ for growing modes at aspect ratio 2 (box a) and aspect ratio 0.8 (box b) at $\lambda = 0.06$, and $Ra = 100 Ra_{crit0}$ with a no-slip rigid upper boundary and a free-slip lower boundary. Solid line: $w(z)$; dotted line: $b(z)$; dashed line: base state \bar{s}_m below the rigid lid.

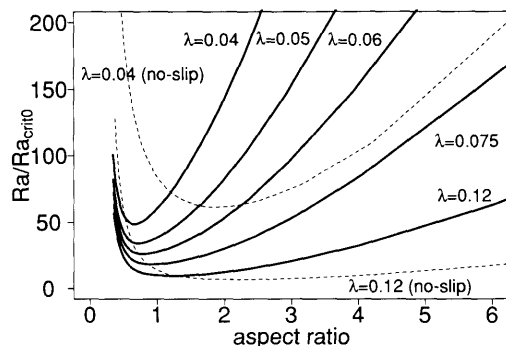


Fig. 7. Solid lines: marginal stability curves for 5 different cooling depths ($\lambda = 0.04, 0.05, 0.06, 0.75, 0.12$), thermodynamic profiles as in (2c), scaled by $Ra_{crit0} = 657$, for the inversion of Fig. 2. Dashed lines: the stability curves for a no-slip rigid upper boundary at $z = 1$ with $\lambda = 0.04$ and $\lambda = 0.12$.

aspect ratio less than 2.3 will be unstable to infinitesimal perturbations. If the inversion is replaced by a no-slip rigid lid (dashed line, Fig. 5), the range of unstable aspect ratios extends to $a = 6$. As the cooling zone deepens, this localization becomes less and less of an advantage, until, for unstable layers deeper than $\lambda = 0.12$, there is little difference between modes driven from cloud top and those that arise from an unstable region spanning the entire layer depth.

The velocity and buoyancy perturbations for two growing modes are shown in Fig. 8 for the same conditions as Fig. 6: $Ra = 100 Ra_{crit0}$, $\lambda = 0.06$, the inversion of Fig. 4, and aspect ratios of $a = 2$ and $a = 0.8$. Compared to a no-slip rigid lid, the inversion-capped layer has both a higher growth rate ($\sigma = 83$, panel b)) for the small aspect ratio mode, and a lower growth rate ($\sigma = 23$, panel a)) for the large aspect-ratio mode at this forcing.

The inversion confers a growth advantage on the small-scale convection (and exacts a penalty for the $a = 2$ mode) by changing the height of the buoyancy perturbation maximum. It has dropped from $z = 0.85$ (panel 6a) to $z = 0.8$ (panel 8a) for $a = 2$, and risen from $z = 0.88$ to $z = 0.9$ for $a = 0.8$ (panel b). Moving the buoyancy perturbation further into the unstable layer in Fig. 8b increases the magnitude of $b(z)$ and the buoyancy production P by 25% compared to the same aspect ratio convection beneath a rigid lid. Dissipation for the $a = 0.8$ mode increases slightly, and there is some buoyancy consumption within the inversion for both modes in Fig. 8, but the cumulative impact of the inversion is to produce more rapidly growing modes at smaller aspect ratios than are generated by the same unstable layer capped by a rigid lid.

These results are not sensitive to the shape of the base state \bar{s}_m ; replacing the exponential with a piecewise-linear base state of equivalent depth and the same inversion strength and thickness preserves the selection of small-aspect ratio modes.

3.3. Sensitivity to inversion strength and inversion depth

We have so far fixed both the inversion strength f_b and the shape functions v_f and α_f which control the transition between the cloud and the inviscid, stable layer. Relaxing the transition depth or reducing the inversion strength can be expected to decrease the impact of the inversion on mode selection, as the buoyancy perturbations associated with the thicker inversions become less tightly defined, and the perturbation maxima are pushed below the radiatively-cooled zone and the buoyancy flux is reduced.

The balloon-borne measurements of Caughey et al. (1982) show the depth of the "entrainment interface layer" separating the turbulent and non-turbulent air near cloud top can vary between 1–10 m, and the effective interface, averaged over small-scale cloud top undulations, may be larger than that. It is also possible that cloud top could exhibit a range of values of α_{cloud} , depending on the details of the entrainment process and the energy and vapor contrasts across the inversion. Changes in the cloud top character of either of these variables will influence (23) primarily through the derivatives $d\alpha/dz$, dv_f/dz . In Fig. 9 we show the sensitive of a_{crit} to a 50% reduction in $d\alpha/dz$, and dv_f/dz , and to variations in the inver-

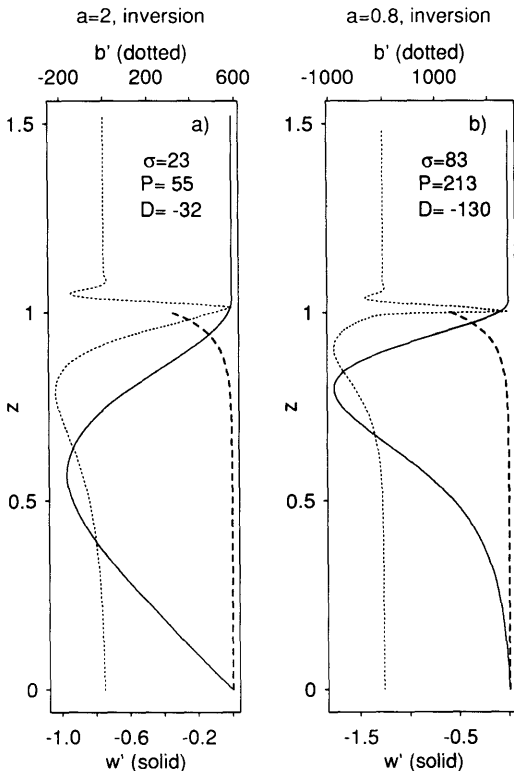


Fig. 8. As in Fig. 6 but for the inversion of Fig. 2 at $\lambda = 0.06$, and $Ra = 100 Ra_{crit0}$. Solid line: $w(z)$; dotted line: $b(z)$; dashed line: base state \bar{s}_m below the inversion.

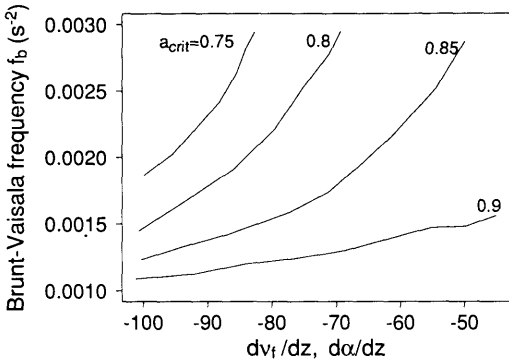


Fig. 9. Contour plot of aspect ratio a as a function of inversion Brunt-Väisälä frequency ($f_b = (g/\theta_{v0}) d\theta_v/dz$ (s^{-2})), and the vertical derivative of the shape functions $dv_t/dz, d\alpha/dz$.

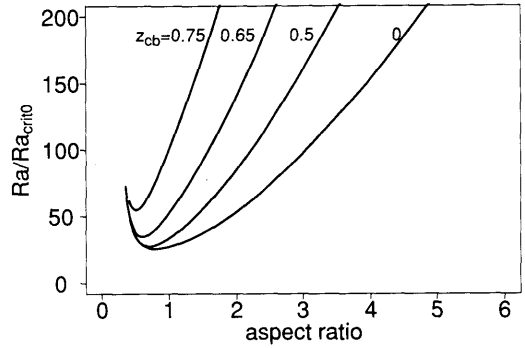


Fig. 10. Marginal stability curves as a function of cloud base height z_b (shown to the left of each curve) for exponential \bar{s}_m profiles with $\lambda = 0.06$, and an inversion strength of 6 K/100 m.

tion strength in the range 2 K/100 m < dT/dz < 8 K/100 m ($0.001 s^{-2} < f_b < 0.003 s^{-2}$). The values of a_{crit} vary by approximately 20% across this range of parameters, with the aspect ratio increasing as the inversion is thickened and weakened. All critical aspect ratios are less than 50% of the critical aspect ratio for a no-slip rigid lid with $\lambda = 0.04$.

3.4. Sensitivity to cloud depth

For simplicity, the base states of Subsection 3.2 had a transition between cloud and clear air only at cloud top, i.e., they were cloudy from the inversion to surface. In the marine boundary layer, observations (e.g., Paluch and Lenschow, 1991; Nicholls and Turton, 1987; Betts, 1989) indicate that the layer is frequently not well-mixed, as solar heating at cloud base decouples the cloud from its source of heat and moisture. As a simple approximation to this situation, we set $\alpha = 0$ below cloud base (see Fig. 2) to force the sub-cloud buoyancy flux to zero. The inversion strength, α and v_r are kept as in Fig. 2, with $\lambda = 0.06$.

Forcing the buoyancy flux to zero in this way introduces an additional penalty for large-aspect ratio modes that extend below the cloud layer. This is apparent from the shift in a_{crit} in Fig. 10; it is reduced from $a_{crit} = 0.81$ to $a_{crit} = 0.53$ as the cloud thickness approaches $\Delta z = 0.25$ ($z_{cb} = 0.75$).

Fig. 11 shows the perturbation modes with cloud base $z_{cb} = 0.7$ and a forcing of 100 Ra_{crit} . These modes can be compared directly with those of Fig. 8: the imposition of a cloud base at $z = 0.7$

has decreased buoyancy production for $a = 2$ from $P = 57$ to $P = 18$, while it is essentially unchanged (from $P = 222$ to $P = 213$) for the smaller $a = 0.8$ mode. With the decoupled cloud base, the mode dissipation at $a = 0.8$ has increased slightly, requiring larger forcing to initiate convection, as indicated by the larger critical Rayleigh numbers in the stability curves of Fig. 10.

4. Discussion

We have examined the impact of the upper boundary condition on the onset of convection in an idealized, radiatively-cooled stratocumulus cloud. This analysis was motivated by observations of pattern-form convection at cloud top, which suggest the presence of a scale-selection mechanism acting to organize updrafts and downdrafts in these clouds. Although the linearized Boussinesq equations cannot represent the fundamentally non-linear interactions that stabilize growing convection at finite amplitude, a linear stability analysis can provide a benchmark for the impact of the upper boundary on the linearly unstable modes. Our results indicate that, for typical inversions overlying an unstable upper cloud layer, the forcing required to initiate convection, and the range of aspect ratios excited at a particular Rayleigh number, are strongly affected by the upper boundary.

By considering only the separable solutions to the linearized Boussinesq equations, we eliminate

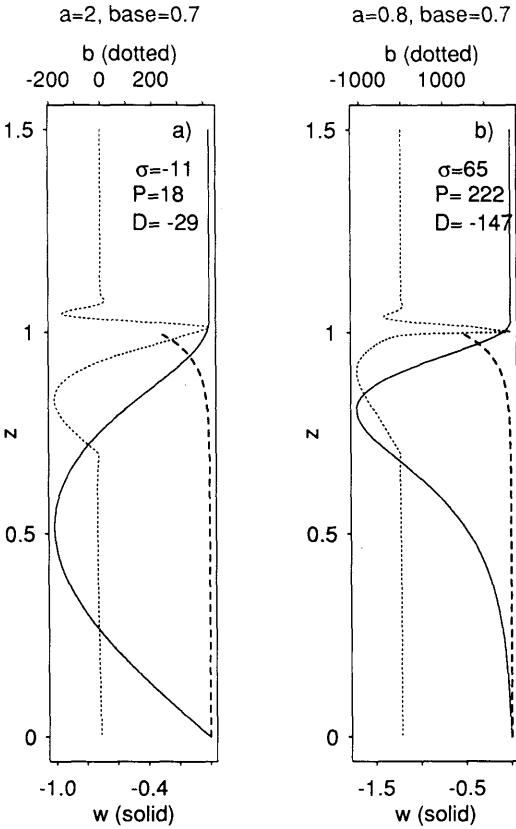


Fig. 11. Non-dimensional perturbations $w(z)$ (solid), and $b(z)$ (dotted), for growing modes on a base state with cloud base at $z = 0.7$, $\lambda = 0.06$, $Ra = 100 Ra_{crit}$. (a) aspect ratio $a = 2$, (b) $a = 0.8$.

the possibility of horizontal transitions between saturated and unsaturated air. Although this is fundamental to the scale selection process in convection in partially cloudy layers (Laufersweiler and Shirer, 1989; Van Delden, 1988), it is not difficult to find unbroken, completely saturated stratocumulus cloud sheets, and we have limited ourselves to these clouds in this analysis. We also assume that the combined effect of the energy and total water fluxes on the layer buoyancy can be represented through a height dependent proportionality constant, α . This is most appropriate for a cloud layer with small surface fluxes of energy and water; the assumption is weakest in the sub-cloud layer, where energy and water perturbations contribute equally to the buoyancy flux.

The perturbation equations do not include

interactions between the velocity perturbations at the inversion and the entrainment of inversion air. This would be a particularly serious omission if entrainment was destabilizing, i.e., if entrainment events released kinetic energy and enhanced turbulence at the inversion. Numerical models of entraining eddies (e.g., Siems and Bretherton, 1992) indicate that, for stratocumulus inversions, this is not the case, and that entrainment consumes the turbulent kinetic energy of the entraining eddies. Our stability analysis complements a model of entrainment across an undulating stratocumulus interface by Breidenthal and Baker (1985) which takes as its input the dominant aspect ratio, a_{crit} and the depth and intensity of the radiative cooling, and predicts the entrainment due to engulfment of inversion air in the valleys between the undulating "hummocks" of wavelength a_{crit} . Intermittent entrainment events located in these valleys would tend to reduce the inversion-cloud density difference and therefore be potentially stabilizing, but Breidenthal and Baker use a simple two-layer model of the undulating interface to show that radiative cooling dominates the layer energetics, and that a passive treatment of the entrainment still produces vertical velocity perturbations that are a close fit with the observations of nocturnal clouds.

Within a range of conditions typical of marine stratocumulus, the neutral stability curves and growing modes presented in our sensitivity tests show that an inversion damps the growth rate of modes with aspect ratios > 1 , and accelerates the growth of smaller aspect ratio modes, relative to a boundary layer capped by a rigid lid. This damping can be large: the growth rate at a forcing of $100 Ra_{crit0}$, an aspect ratio of 3 and a cooling length $\lambda = 0.05$ is $\sigma = 39$ for a free-slip lid, $\sigma = 11$ for a no-slip lid, and to $\sigma = -16$ for an inversion.

In addition to exacting a penalty from large aspect ratio modes, a strong inversion produces more rapidly growing small aspect ratio modes, with perturbation profiles localized near the top of the radiatively cooled layer. This means that the layer will become unstable at slightly lower Rayleigh numbers for an inversion than for a rigid lid. For $\lambda = 0.05$, convection under the capping inversion of Fig. 7 begins at $Ra_{crit} = 34 Ra_{crit0}$ and $a_{crit} = 0.73$, compared with $Ra_{crit} = 36 Ra_{crit0}$ and $a_{crit} = 2.0$ for a rigid lid. Associating this forcing with a critical energy difference $c_p \Delta T_v$ requires a

value for the eddy viscosity ν_0 ; taking $5 < \nu_0 < 10 \text{ m}^2 \text{ s}^{-1}$ yields a convective forcing $0.03 \text{ K} < \Delta T_v < 0.1 \text{ K}$, close to the buoyancy contrast observed in the convective plumes of Fig. 1.

Although the calculation of the aspect ratio actually selected by cloud top convection requires a non-linear treatment, these results indicate that the cloud-top boundary should play an important role in determining an energetically favored length scale for the convection. If the Rayleigh number required to initiate convection is close to the forcing available in radiatively cooled layer clouds, the possibility of scale selection is increased, as only a relatively narrow band of modes can become linearly excited and grow. The marginal stability curves shown above suggest that the aspect ratio of these unstable modes will be close to 1, in agreement with the observations of organized cloud top convection presented in Section 1.

There is relatively little observational evidence on conditions that favor a dominant convective length scale at cloud top. The results presented above (e.g., Fig. 7) suggest that the range of aspect ratios of linearly unstable modes increases rapidly as the unstable layer deepens. Thus, strong surface fluxes could make the process of scale selection more difficult, as the depth of the unstable layer is increased, the critical Rayleigh number is decreased, a greater range of unstable linear modes can grow, and the layer is moved farther away from the small amplitude regime near the critical Rayleigh number. Opposing this is the tendency for sub-cloud stabilization and decoupling to produce small aspect ratio convection as demon-

strated in Subsection 3.4. A layer at the beginning of a transition from solid stratocumulus to broken cumulus might be expected to produce convection at smaller aspect ratios for this reason, but once the cloud layer begins to break up the impact of horizontal transitions between cloud and clear air would dominate the layer thermodynamics and dynamics.

Ideal conditions under which to find scale selection might occur during the evening transition from solar heating and longwave cooling to cooling alone in a fully cloud boundary layer. At mid-latitudes a 50 W m^{-2} reduction in the downward solar flux can occur within 45 min in the early evening. This change is localized to the upper 100 m of the cloud, and could drive the layer Ra_{crit} upward in the absence of destabilizing surface fluxes. The observations of convective organization by both Caughey and Kitchen (1984), (Fig. 1), and Nicholls and Leighton (1986) approximate these evening conditions.

5. Acknowledgments

We are grateful to M. Baker, C. Bretherton and G. McBean for many helpful discussions and comments on earlier drafts of this article and to the helpful comments of two anonymous reviewers. Portions of this work were supported by the National Science Foundation under Grant ATM-8304670 and by the National Science and Engineering Research Council of Canada.

REFERENCES

- Albrecht, B. A., Randall, D. A. and Nicholls, S. 1988. Observations of marine stratocumulus during FIRE. *Bull. Amer. Meteor. Soc.* **69**, 618–626.
- Bakan, S. 1982. Radiative influence on small scale convection within stratus cloud layers. In: *Cloud dynamics*, Agee, E. and Asai, T., eds. D. Reidel, 43–56.
- Betts, A. K. 1990. Diurnal variation of California coastal stratocumulus from two days of boundary layer soundings. *Tellus* **42A**, 302–304.
- Breidenthal, R. E. and Baker, M. B. 1985. Convection and entrainment across stratified interfaces. *J. Geophys. Res.* **90**, 13055–13062.
- Bretherton, C. S. 1987. A theory for nonprecipitating moist convection between two parallel plates. Part I: thermodynamics and “linear” solutions. *J. Atmos. Sci.* **44**, 1809–1827.
- Carruthers, D. J. and Moeng, C. H. 1987. Waves in the overlying inversion of the convective boundary layer. *J. Atmos. Sci.* **44**, 1801–1808.
- Caughey, S. J., Crease, B. A. and Roach, W. T. 1982. A field study of nocturnal stratocumulus: II. turbulence structure and entrainment. *Quart. J. Roy. Meteor. Soc.* **108**, 125–144.
- Caughey, S. J. and Kitchen, C. K. 1984. Simultaneous measurements of the turbulent and microphysical structure of nocturnal stratocumulus cloud. *Quart. J. Roy. Meteor. Soc.* **110**, 13–34.
- Conte, S. D. 1969. The numerical solution of linear boundary value problems. *SIAM Review* **8**, 309–317.
- Fiedler, B. 1984. The mesoscale stability of entrainment into cloud-topped mixed layers. *J. Atmos. Sci.* **41**, 92–101.

- Hanson, H. P. and Derr, V. E. 1987. Parameterization of radiative flux profiles within layer clouds. *J. Climate Appl. Meteor.* **26**, 1511–1521.
- Hurle, D. T. J., Jakeman, E. and Pike, E. R. 1967. On the solution of the bérard problem with boundaries of finite conductivity. *JFM* **30**, 469–475.
- Koraćin, D. and Rogers, D. 1990. Numerical simulations of the response of the marine atmosphere to ocean forcing. *J. Atmos. Sci.* **47**, 592–611.
- Laufersweiler, M. J. and Shirer, H. N. 1989. A simple dynamical model of a stratocumulus-topped boundary layer. *J. Atmos. Sci.* **46**, 1133–1153.
- Lilly, D. K. 1968. Models of cloud-topped mixed layers under a strong inversion. *Quart. J. Roy. Meteor. Soc.* **94**, 292–309.
- Mahrt, L. 1986. On the shallow motion approximations. *J. Atmos. Sci.* **43**, 1036–1044.
- Moeng, C. H. 1986. Large-eddy simulation of a stratus-topped boundary layer. Part I: Structure and budgets. *J. Atmos. Sci.* **43**, 2886–2900.
- Moeng, C.-H. and Schumann, U. 1991a. Plume fluxes in clear and convective boundary layers. *J. Atmos. Sci.* **48**, 1746–1757.
- Moeng, C.-H. and Schumann, U. 1991b. Composite structure of plumes in stratus-topped boundary layers. *J. Atmos. Sci.* **48**, 2280–2291.
- Moyer, K. A. and Young, G. S. 1991. Observations of vertical velocity skewness within the marine stratocumulus-topped boundary layer. *J. Atmos. Sci.* **48**, 403–410.
- Nicholls, S. 1989. The structure of radiatively driven convection in stratocumulus. *Quart. J. Roy. Meteor. Soc.* **115**, 487–512.
- Nicholls, S. and Leighton, J. 1986. An observational study of the structure of stratiform cloud sheets: Part I. Structure. *Quart. J. Roy. Meteor. Soc.* **112**, 431–460.
- Nicholls, S. and Turton, J. D. 1986. An observational study of the structure of stratiform cloud sheets: Part II. Entrainment. *Quart. J. Roy. Meteor. Soc.* **112**, 461–480.
- Paluch, I. R. and Lenschow, D. H. 1991. Stratiform cloud formation in the marine boundary layer. *J. Atmos. Sci.* **48**, 2141–2158.
- Randall, D. A. 1980. Conditional instability of the first kind upside-down. *J. Atmos. Sci.* **41**, 402–413.
- Roach, W. T., Brown, R., Caughey, S. J., Crease, B. A. and Slingo, A. 1982. A field study of nocturnal stratocumulus: I. Mean structure and budgets. *Quart. J. Roy. Meteor. Soc.* **108**, 103–123.
- Sasaki, Y. 1970. Influences of thermal boundary layer on atmospheric cellular convection. *J. Meteor. Soc. Japan* **48**, 492–501.
- Siems, S. T. and Bretherton, C. S. 1992. A numerical investigation of cloud-top entrainment instability and related experiments. *Quart. J. Roy. Meteor. Soc.* **118**, 787–818.
- Siems, S. T., Lenschow, D. H. and Bretherton, C. S. 1993. A numerical study of the interaction between stratocumulus and the air overlying it. *J. Atmos. Sci.* **50**, 3663–3676.
- Turton, J. D. and Nicholls, S. 1987. A study of the diurnal variation of stratocumulus using a multiple mixed layer model. *Quart. J. Roy. Meteor. Soc.* **113**, 969–1009.
- Van Delden, A. 1988. On the flow-pattern of shallow atmospheric convection. *Cont. Atmos. Phys.* **61**, 169–186.